Quantification of three-dimensional surface derormation using global digital image correlation

Please check the document version of this publication:

• A submitted manuscript is the version of the article upon submission and before peer-review. There can be important differences between the submitted version and the official published version of record. People interested in the research are advised to contact the author for the final version of the publication, or visit the DOI to the publisher's website.
• The final author version and the galley proof are versions of the publication after peer review.
• The final published version features the final layout of the paper including the volume, issue and page numbers.

Link to publication

Quantification of Three-Dimensional Surface Deformation using Global Digital Image Correlation

**J. van Beeck · J. Neggers · P.J.G. Schreurs ·
J.P.M. Hoefnagels · M.G.D. Geers**

Abstract A novel method is presented to experimentally quantify evolving surface profiles. The evolution of a surface profile is quantified in terms of in-plane and out-of-plane surface displacements, using a Finite Element based Global Digital Image Correlation procedure. The presented method is applied to a case study, i.e. deformation-induced surface roughening during metal sheet stretching. The surface roughness was captured *in-situ* using a confocal optical profiler. The Global Digital Image Correlation method with linear triangular finite elements is applied to track the three-dimensional material movement from the measured height profiles. The extracted displacement fields reveal the full-field kinematics accompanying the roughening mechanism. Local deviations from the (average) global displacements are the result of the formation, growth, and stretching of hills and valleys on the surface. The presented method enables a full-field quantitative study of the surface height evolution, i.e. in terms of tracked surface displacements rather than average height values such as Root-Mean-Square or height-height correlation techniques. However, the technique does require that an initial surface profile, i.e. contrast, is present and that the contrast change between two measurements is minimal.

J. van Beeck (✉)
Materials innovation institute (M2i), Delft, The Netherlands
e-mail: J.vanBeeck@m2i.nl

J. van Beeck · J. Neggers · P.J.G. Schreurs · J.P.M. Hoefnagels ·
M.G.D. Geers
Department of Mechanical Engineering, Eindhoven
University of Technology, Den Dolech 2,
5612 AZ Eindhoven, The Netherlands

J.P.M. Hoefnagels
e-mail: J.P.M.Hoefnagels@tue.nl

Introduction

A change in surface height profile is characteristic for many mechanical phenomena. For example, during cyclic fatigue loading of many metals, surface relief shows steps in the outer surface due to the extrusion and intrusion of plastic slip bands [1, 2]. Likewise, many creep experiments reveal significant grain boundary sliding, causing changes in the local surface height [3]. Also, in a uniaxial tensile test, the surface height profile of a metal locally changes, due to the crystallographic orientation differences between grains and dislocations escaping at the free surface [4, 5]. As a final example, surface height profile evolution occurs in contact and wear problems [6]. In all these examples, pronounced local variations in the surface height appear. Quantifying the in-plane and out-of-plane evolution of the surface height profile can provide valuable information on the underlying mechanisms.

In the case of the deformation-induced surface roughening, which is found in many metals, it may be important to accurately determine the local deformation at the metal surface. This is particularly the case for polymer-coated steels used for food and beverage packaging (Fig. 1). This material is deformed in an industrial process using subsequent deep-drawing, deep-redrawing, and wall ironing to produce a can or canister. Compared to the traditional production process, which consists of first producing a steel can and then applying the coating, the use of pre-coated packaging steel leads to not only a 30 % reduction of energy consumption and CO_2 emission, and a reduction of process
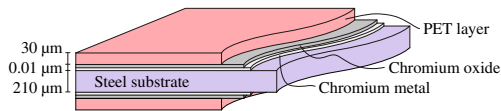
Fig. 1 Different material layers in a polymer coated steel (after [11])

water consumption, but also a reduction of solid waste to practically zero [7]. Unfortunately, however, pre-coating the steel comes with a number of challenges, since the coating undergoes the same deformation steps as the steel. As previous work by Boelen et al. [8], Van den Bosch et al. [9] and Fedorov et al. [10] showed, the interface adhesion is strongly influenced by deformation, and even though damage is often not optically visible after can production, the damage may become apparent during the prolonged shelf-life of the product. This is not desirable, since application for food packaging demands that the material does not exhibit any damage on the inside of the can, even after a relatively long shelf-life period, since this triggers corrosion and compromises the quality of the can content [8, 9, 11].

A possible cause of interface damage is the deformation-induced heterogeneous change in surface height of the steel. It is well known that the free surface of a polycrystalline metal roughens when it is deformed, due to crystallographic orientation differences between grains and other plasticity related phenomena. This roughening occurs over a wide range of length scales, ranging from the nanoscale to the size of multiple grains, depending on deformation conditions and material properties (see Fig. 2) [4]. Many different techniques for visualizing a surface topography are found in literature, e.g. stylus-type techniques, Atomic Force Microscopy (AFM), optical techniques (confocal and interferometry) [4–6, 9, 12].

A surface topography, and the change thereof, is typically characterized by average height values, e.g. Root-Mean-Square (RMS), average (AVG), and maximum peak-to-valley (MPV) [4–6, 12]. Another characterization method is the statistical height-height correlation method [9, 13].

While these techniques give insight into the amplitude of the height change and how the (average) height evolves, they do not provide actual information on local material deformation. This shortcoming was circumvented by Van Tijum et al. [13]. In contrast to using local surface deformations, they used a numerically generated out-of-plane deformation and a global in-plane deformation to predict the interface integrity of a polymer-coated steel. However, while these simulations give valuable insight into the effect of roughening on the adhesion between the polymer and the steel, the authors did not take into account the local evolving deformation fields that resulted from the steel roughening (e.g., due to the evolving rotation of grains).

This paper presents a new methodology, which uses Global Digital Image Correlation (GDIC) to track three-dimensional surface deformations from evolving surface height profiles. The method is independent of the measurement technique used to obtain the profiles, and the methodology is verified using well-defined displacement fields and measured height profiles of a steel surface. A case study was used to validate the technique, i.e. the deformation-induced surface roughening of a polymer-coated steel during a uniaxial tensile test. The surface height profile is captured *in-situ* using confocal microscopy. This case study was chosen because of its complexity, i.e. a) the initial surface roughness of the steel is smooth in the rolling direction of the steel, creating a low (height) contrast image in this direction, b) the steel shows Lüder-bands in a uniaxial tensile test, which is accompanied by a sudden change in the surface profile, c) the surface profile continuously changes when the deformation is increased, due to the deformation-induced roughening, and d) compared to other profilometers (e.g. AFM), the confocal profiler has a relatively low number of pixels. Confocal microscopy is used in the presented work, because the technique is well suited for measuring an evolving surface height profile *in-situ*. Other techniques that can be applied within the presented framework are, for example, AFM, stereo-correlation microscopy, and X-ray tomography. These techniques are also capable of measuring a surface profile.

The paper is organized as follows. First, in section "Global Digital Image Correlation", the GDIC method is explained in detail, followed by a derivation of the equations and some aspects regarding its implementation. In the next section, an extensive verification analysis of
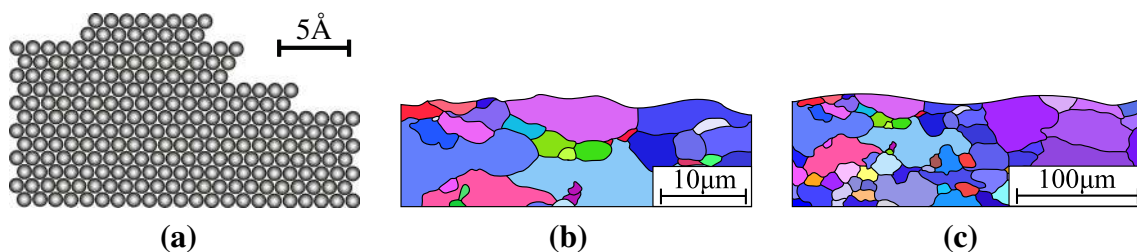

Fig. 2 Schematic examples of roughening phenomena, (**a**) sub-grain roughening (e.g. crystallographic slip steps) and (**b**) grain-scale roughening (*orange peel*) (**c**) poly-grain-scale roughening (*ridging*); *scale-bars* indicate the typical scale of the phenomenon

the GDIC method is given for several well-defined virtual experiments. The validation experiments performed with the polymer-coated steel are discussed in section "Proof-of-Principle Experiments". The paper ends with some concluding remarks.

The following notations are adopted throughout the paper. A vector is denoted by **a**. The inner product is defined as $\mathbf{a} \cdot \mathbf{b} = a_i b_i$. The unit vectors of a Cartesian basis are $\mathbf{e}_i$; $i = x, y, z$. A matrix and a column are denoted by $\underline{A}$ and $\underline{a}$, respectively. A matrix or column average is denoted by $\langle \ldots \rangle$ and the absolute value by $|\ldots|$.

Global Digital Image Correlation

Background and Motivation

Digital Image Correlation (DIC) is a well-established method to extract material displacement from images. Within the framework of DIC there are two methodologies, i.e. "local" DIC and "global" DIC (GDIC) [14]. Local DIC is the traditional, older, and widely used method, while GDIC was more recently developed and is less well-known. The difference between the two methodologies is that in GDIC some properties of the kinematics of the problem are assumed to be known (e.g. continuity of the displacement field), and the displacement field is calculated using the entire field of view (FoV), rather than local facet information. The fundamental basis of DIC is the conservation of brightness, i.e. the image contrast of a material point does not change between two images.

However, the assumption of brightness conservation is almost always violated when using experimentally measured images. This violation occurs, for example, due to (a) the formation of slip steps on a steel surface in the presence of large deformations, affecting light reflection, (b) out-of-plane sample motion as a result of bending or the Poisson's Ratio, (c) the camera and sample not being perpendicular, (d) fluctuations in the light-source, (e) noise stemming from the used camera, (f) geometric distortions from SEM scanning, (g) pattern evolution, and more [15–18].

As such, a change in grayscale or height value does not strictly relate to motion or deformation of the material in the experimental images. To reduce or deal with this change in image contrast, several methods were developed, e.g averaging several images, or applying corrections functions, or incrementally applying the deformation to prevent large changes between two images, or by inserting some kinematics into the solution procedure [15–17, 19]. The latter method is used in GDIC. Hild and Roux [20] have shown that Global DIC generally out-performs local DIC due to the assumed kinematics, which reduce the sensitivity to changes in brightness and restricts the solution space. In all cases, an optimization algorithm is applied to find the displacement field iteratively, minimizing the contrast difference between the two images.

Measured surface height profiles are two-dimensional (or one-dimensional) images, where the pixel value indicates a local height value at the pixel location in a spatial frame. This requires a DIC method capable of extracting the three-dimensional material displacements from these "Quasi-3D" spatial height images. The available DIC methodologies have been developed for two-dimensional and three-dimensional (optical and SEM) images (also known as *Digital Volume Correlation*), with gray-valued pixels or voxels, respectively [16, 21]. So far, exploiting spatial height profiles to extract material displacement fields has only been done by Vendroux et al. [22] to obtain the three-dimensional displacement fields from Scanning Tunneling Microscopy (STM) data. The local DIC methodology was adapted to allow for out-of-plane movement by adding the out-of-plane displacement to the degrees-of-freedom. As a result, the three-dimensional displacement field could be extracted from the STM profiles. The method was applied to rigid body rotation. However, no (gradual) change in roughness pattern was tracked using this methodology. Later, Knauss et al. [23] showed that including the out-of-plane displacement is vital when using height profiles to determine the in-plane displacements. Furthermore, height profilometry has also been used in the GDIC method to determine the stress intensity factors around a crack tip from AFM height profiles by Han et al. [24]. The method used was Integrated DIC (I-DIC), where a-priori kinematic information of the crack tip intensity factors is used in the GDIC solution procedure. This a-priori information is typically not available when attempting to determine the material displacements from spatial height profiles. It is not known beforehand where material points will move, since this depends on many different properties, e.g. in the case of deformation-induced roughening this depends on grain orientation and size, material, etc. Thus, I-DIC methods cannot be applied trivially here. A Finite Element based GDIC method (FE-DIC) does not require a-priori knowledge of the kinematics, except for the assumed C0 continuity of the used finite element shape functions. A Quasi-3D FE-DIC method allows tracking of material displacements in evolving surface height profiles. FE-DIC has been applied before on two-dimensional optical images [25–27]; however, the method has not yet been extended to Quasi-3D height profiles.

Quasi-3D FE-DIC for Spatial Height Profiles

The goal in Quasi-3D FE-DIC is to identify the displacement field, $\mathbf{u}(\mathbf{x}_0) = \mathbf{u}_{xy}(\mathbf{x}_0) + u_z(\mathbf{x}_0)\mathbf{e}_z$, with $\mathbf{u}_{xy}(\mathbf{x}_0) = u_x(\mathbf{x}_0)\mathbf{e}_x + u_y(\mathbf{x}_0)\mathbf{e}_y$, that correlates two height images, namely a reference image, $f(\mathbf{x}_0)$, and a "deformed" image,

$g(\mathbf{x}) = g(\mathbf{x}_0 + \mathbf{u}_{xy}(\mathbf{x}_0))$. Here, an image in mathematical terms is a matrix of spatial pixel positions, $\mathbf{x}_0$ or $\mathbf{x}$, and a matrix of scalar pixel *height values*. This goal, schematically shown in Fig. 3(a), can be written at the pixel level as

$$f(\mathbf{x}_0) - g(\mathbf{x}_0 + \mathbf{u}_{xy}(\mathbf{x}_0)) + u_z(\mathbf{x}_0) = \eta(\mathbf{x}_0), \quad \forall \mathbf{x}_0 \in \mathscr{B}_0, \quad (1)$$

where $\eta(\mathbf{x}_0)$ contains the residual difference between the two images, e.g. measurement noise, and $\mathscr{B}_0$ is the region of interest. The traditional assumption of brightness conservation is thus redefined to allow for some *minor* changes in the surface height profile, i.e. the image contrast.

The goal is thus to find the displacement field that minimizes this residual difference within $\mathscr{B}_0$. Thus, equation (1) is set up for each pixel within $\mathscr{B}_0$. For each pixel with one measured quantity (i.e. its height), there are three unknowns (i.e. u_x, u_y and u_z). In order to find the displacement field, a finite element discretization is applied (see Fig. 3(b)), which greatly reduces the number of unknowns by assuming that the kinematics can be captured by means of the adopted finite element discretization.

In each element, the displacement $\mathbf{u}(\mathbf{x}_0)$ of an internal point is interpolated between the displacement, $\underset{\sim}{u}$, of n nodal points, using n shape functions, φ, which are a function of the local isoparametric coordinate, ξ,

$$\mathbf{u}(\mathbf{x}_0) \approx \sum_{k=1}^{n} \varphi_k(\xi(\mathbf{x}_0))\mathbf{u}_k = \underset{\sim}{\varphi}^{\mathrm{T}}(\xi(\mathbf{x}_0))\underset{\sim}{u}. \quad (2)$$

After assembling all the elements, and taking into account the continuity of the nodal displacements, the total system (in components) reads

$$\underset{\sim}{\eta}(\underset{\sim}{x}_0) = \underset{\sim}{f}(\underset{\sim}{x}_0) - \underset{\sim}{g}(\underset{\sim}{x}_0 + \underline{M}(\underset{\sim}{x}_0)\underline{A}\underset{\sim}{u}) + \underline{M}(\underset{\sim}{x}_0)\underline{B}\underset{\sim}{u}, \quad (3)$$

$$\underset{\sim}{u}_{xy} = \underline{A}\underset{\sim}{u} \quad \& \quad \underset{\sim}{u}_z = \underline{B}\underset{\sim}{u}. \quad (4)$$

The size of $\underset{\sim}{f}$, $\underset{\sim}{g}$ and $\underset{\sim}{\eta}$ is $(p \times 1)$, of $\underline{M}(\underset{\sim}{x}_0)$ is $(p \times 3n)$, of $\underline{A}$ and $\underline{B}$ is $(3n \times 3n)$ and of $\underset{\sim}{u}$ is $(3n \times 1)$, where p is the number of pixels. In general $3n \ll p$, whereby a solution

can be obtained via the least-squares method, minimizing the error Φ with respect to the displacement field, i.e.

$$\underset{\underset{\sim}{u}}{\mathrm{argmin}}(\Phi(\underset{\sim}{u})), \quad \text{with } \Phi(\underset{\sim}{u}) = \underset{\sim}{\eta}(\underset{\sim}{u})^{\mathrm{T}}\underset{\sim}{\eta}(\underset{\sim}{u}). \quad (5)$$

Minimization using equation (3) gives

$$\underset{\sim}{\Psi}(\underset{\sim}{u}) = \frac{\partial \Phi}{\partial \underset{\sim}{u}} = 2\left(\frac{\partial \underset{\sim}{\eta}}{\partial \underset{\sim}{u}}\right)^{\mathrm{T}}\underset{\sim}{\eta}(\underset{\sim}{u}) = \underset{\sim}{0}. \quad (6)$$

To solve this non-linear equation in the degrees-of-freedom, $\underset{\sim}{u}$, an iterative procedure is applied. First, equation (6) is linearized with respect to the degrees-of-freedom,

$$\underset{\sim}{u}^{(i+1)} = \underset{\sim}{u}^{(i)} + \delta\underset{\sim}{u}, \quad (7)$$

$$\underset{\sim}{\Psi}^{(i+1)} = \underset{\sim}{\Psi}^{(i)} + \frac{\partial \underset{\sim}{\Psi}^{(i)}}{\partial \underset{\sim}{u}}\delta\underset{\sim}{u} = \underset{\sim}{0}. \quad (8)$$

Here, i is the iteration index. Expressions for the separate contributions in equation (8) are

$$\underset{\sim}{\Psi}^{(i)} = -2\underline{K}^{(i)}(\underset{\sim}{x}_0)\left(\underset{\sim}{f}(\underset{\sim}{x}_0) - \underset{\sim}{g}^{(i)}(\underset{\sim}{x}_0)\right), \quad (9)$$

with

$$\underset{\sim}{g}^{(i)}(\underset{\sim}{x}_0) = \underset{\sim}{g}\left(\underset{\sim}{x}_0 + \underline{M}(\underset{\sim}{x}_0)\underline{A}\underset{\sim}{u}^{(i)}\right) - \underline{M}(\underset{\sim}{x}_0)\underline{B}\underset{\sim}{u}^{(i)}, \quad (10)$$

$$\begin{aligned}\frac{\partial \underset{\sim}{\eta}^{(i)}}{\partial \underset{\sim}{u}} &= -\frac{\partial \underset{\sim}{g}^{(i)}}{\partial \underset{\sim}{x}}\frac{\partial \underset{\sim}{x}}{\partial \underset{\sim}{u}} + \underline{M}(\underset{\sim}{x}_0)\underline{B}, \\ &= -\nabla\underset{\sim}{g}^{(i)}(\underset{\sim}{x}_0)\underline{M}(\underset{\sim}{x}_0)\underline{A} + \underline{M}(\underset{\sim}{x}_0)\underline{B}, \\ &= -\underline{K}^{(i)}(\underset{\sim}{x}_0), \end{aligned} \quad (11)$$

and

$$\frac{\partial \underset{\sim}{\Psi}^{(i)}}{\partial \underset{\sim}{u}} = -2\underline{K}^{(i)\mathrm{T}}(\underset{\sim}{x}_0)\frac{\partial \underset{\sim}{\eta}^{(i)}}{\partial \underset{\sim}{u}} = 2\underline{K}^{(i)\mathrm{T}}(\underset{\sim}{x}_0)\underline{K}^{(i)}(\underset{\sim}{x}_0). \quad (12)$$

Note that matrix $\underline{K}^{(i)}(\underset{\sim}{x}_0)$ contains the iterative gradient, $\nabla\underset{\sim}{g}^{(i)}(\underset{\sim}{x}_0)$, which is a surface gradient, i.e. $\nabla g \cdot \mathbf{e}_z = 0$. Substituting equations (9) and (12) into equation (8) and rewriting yields

$$\delta\underset{\sim}{u} = \left(\underline{K}^{(i)\mathrm{T}}\underline{K}^{(i)}\right)^{-1}\underline{K}^{(i)\mathrm{T}}\left(\underset{\sim}{f} - \underset{\sim}{g}^{(i)}\right), \quad (13)$$

Fig. 3 Problem description

(a) Schematic of the problem to be solved

(b) Element discretization
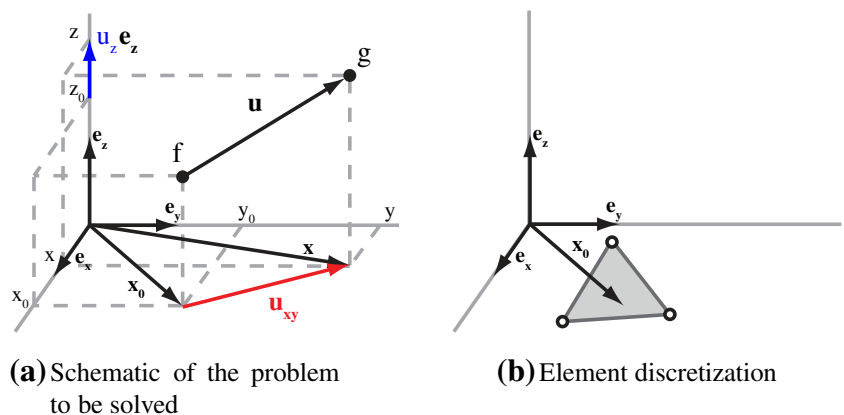
where $(\underline{x}_0)$ was omitted for clarity. To save on computational cost, the iterative gradient, $\underline{\nabla} g^{(i)}(\underline{x}_0)$ in $\underline{K}^{(i)}(\underline{x}_0)$ is replaced by $\underline{\nabla} f(\underline{x}_0)$, which does not require iterative updating, since it does not depend on the displacement field. This replacement leads to a slower convergence rate, as the gradients are only equal when the iterative solution approaches the real solution, near the end of the iterative procedure.

Image Coarsening

As mentioned in the derivation of the GDIC system of equations, the solution is found iteratively. This procedure requires that the displacement is smaller than the dominant correlation length in the roughness pattern, e.g. the grain size. Thus, an adequate initial guess is required in order to converge to the correct solution. This is accomplished by creating so-called "*coarse grained images*" [25]. The two images, $f(\mathbf{x}_0)$ and $g^{(i)}(\mathbf{x}_0)$, are coarsened using so-called "*superpixels*" consisting of 2×2, 4×4, 8×8, etc pixels. This coarsening eliminates the small-scale fluctuations. First, the system is solved for the largest superpixel size, which gives a coarse approximation of the displacement field. This field is next used as an initial guess for the second-largest superpixel size, and so on, until the original image is used. To keep the number of pixels within each element constant, a new mesh is used in each coarse grained image. All the presented results are obtained using three coarsening steps, i.e. the maximum superpixel size was set to 8×8 pixels.

Finite Element Discretization

The finite elements used in the current framework can in principle be taken arbitrarily, but the choice made, and the discretization used, do control the constraints on the kinematics of the field to be identified. In all of the following examples and results, linear triangular finite elements are used.

Following [20], the elements of the edges of the FoV are increased in size, such that the corner and edge elements contain four and two times more pixels than the inner elements, respectively. This increases the stability of the FE-DIC calculation, due to the reduction in degrees-of-freedom per pixel in the edge elements.

Verification Analysis

To gain insight into the quality and efficiency of the method and its implementation, several (virtual) experiments are performed on height profiles characteristic for the problem presented in section "Proof-of-Principle Experiments". Different mesh sizes are used to correlate the displacements and to study the discretization influence.

Two height profiles are used as image $f(\mathbf{x}_0)$ in the verification analysis, namely the initial and final roughness profile of a steel deformed by tension. These profiles were obtained using the experimental setup of the proof-of-principle experiments, described in section "Methodology". The height profiles are shown in Fig. 4. Note that these two profiles were obtained on different parts of the tensile sample. The initial roughness pattern (Fig. 4(a)) clearly shows (horizontal) grooves induced by rolling steel sheet material, while the final roughness pattern (Fig. 4(b)) is dominated by the deformation-induced roughness. Yet, the initial surface roughness pattern remains visible. The difference between these patterns is large and it needs to be verified if the implemented FE-DIC method properly handles this.

First, the error due to measurement noise of the experimental setup, combined with the correlation procedure, is investigated. To this purpose, multiple height measurements are performed on the same location of an undeformed and deformed steel tensile sample. These profiles are then used as images $f(\mathbf{x}_0)$ and $g(\mathbf{x})$ to calculate the displacement field, i.e. two undeformed or two deformed profiles.

The resulting deviation from zero displacement due to the measurement noise, as calculated by the correlation algorithm, for different mesh sizes is shown in Fig. 5(a). The error increases with decreasing element size (reduced number of pixels per element). The increased number of degrees-of-freedom increases the sensitivity to noise in the FE-DIC calculation. The errors in the x and y displacement are noticeably larger than the error in the z displacement. This is because a) no interpolation is required for a displacement in z direction in order to obtain the iterative deformed image $\tilde{g}(\mathbf{x}_0)$, b) the resolution in z is much higher (order of 20 nm compared to 332 nm in x and y), and c) the gradient is a surface gradient and thus only defined in-plane.

Comparing the calculated error in the x and y displacement for the initial surface roughness shows that the error in x is larger. This is explained by the fact that the roughness profile is initially smoother in x direction (RD) than in y direction (TD), see Fig. 4(a). This difference in error is smaller in the case of the final roughness profile, as the roughness profile is then nearly identical in both directions.

The mean error remains below 10 % of the pixel dimension (332 nm) in both cases, which is relatively small, i.e. in the order of the measurement noise (∼20 nm), considering the large number of degrees-of-freedom in the Quasi-3D FE-DIC method.

Next, the error as a result of the interpolation algorithms used in the FE-DIC calculation is investigated. This is accomplished by virtually displacing the two roughness profiles (Fig. 4(a) and (b)) uniformly by 166 nm (half the pixel dimension) simultaneously in x, y and z, creating two new (virtually deformed) images, g. This displacement is a

Fig. 4 Two height profiles of a packaging steel, (**a**) the initial rolling roughness, and (**b**) the roughness after a tensile test close to fracture; the profiles are used in the verification analysis as reference image $f(\mathbf{x}_0)$; dimensions are in microns; *horizontal* and *vertical direction* correspond to the x and y directions, respectively; *colors* indicate the local height value

(a) Initial roughness   **(b)** Final roughness
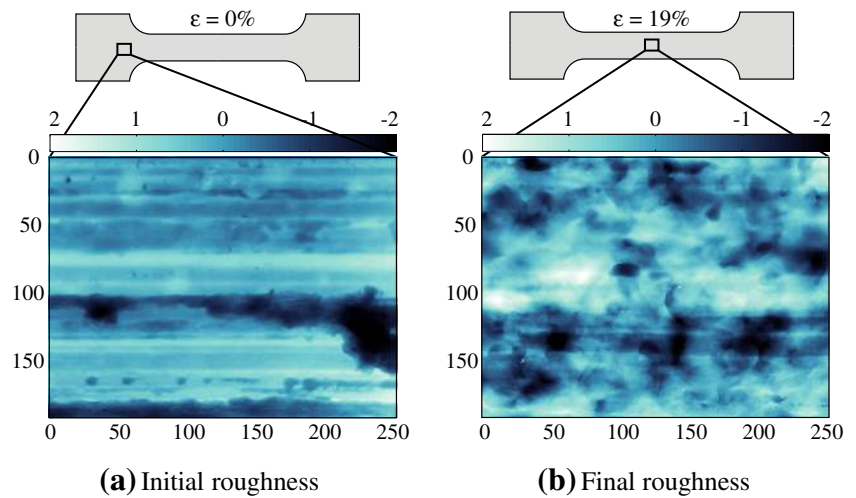
worst case scenario for any interpolation algorithm [14, 25]. This deformed image is then used in the FE-DIC calculation. The resulting error, presented in Fig. 5(b), contains two contributions, 1) the error due to the interpolation used to obtain the deformed image, and 2) the error due to the iterative interpolation required to obtain the displacement fields in the FE-DIC calculation.

The results clearly show that the calculated displacements in the FE-DIC algorithm become less accurate when the element size is decreased. The explanation lies in the increase of the number of degrees-of-freedom (nodes) in the system. This increases the sensitivity to errors in the interpolation algorithm. Similar to the error due to measurement noise, the in-plane displacements (x, y) are more sensitive to the errors in the interpolation compared to the out-of-plane displacement (z). The error for the initial and final roughness profiles, in this case, shows a similar trend and value. Compared to the error found in the analysis of the experimental setup, the error is smaller (less than 2 %), since the displacements used to construct $g(\mathbf{x}_0)$ were virtual and noise-free.

So far, only rigid body displacements were used to characterize the experimental error and interpolation error. A more realistic displacement field, including locally heterogeneous deformations at the surface, is investigated next. The virtual displacement field prescribed, again simultaneously, to the roughness profiles (Fig. 4(a) and (b)) is shown in Fig. 6(left). To simulate measurement noise, random white noise with an amplitude of 20 nm was added to the virtually displaced height profile.

The resulting error is shown in Fig. 5(c). The trends in the error for the x and y directions are similar. Decreasing the element size initially decreases the error value to a minimum. Further decrease of the element size once more increases the error. Smaller elements can more accurately describe the prescribed complex non-linear displacement

field. However, the interpolation error and noise sensitivity become increasingly dominant upon further reduction of the element size.

A different minimum results when comparing the errors in the x and y displacement for the initial surface profile. In y direction (TD), the minimum is found at approximately 450 pixels per element (30 pixels in each direction), while no clear minimum error is visible in x direction (RD). This difference is due to the smoothness of the initial roughness profile in x direction, see Fig. 4(a). Comparing the error in the z displacement with the errors in x and y displacement once again confirms that the error in z is significantly smaller.

The calculated displacement fields for the deformed reference image (Fig. 4(b)) and a mesh containing approximately 450 pixels per element (near the optimum) are shown in Fig. 6(right). Comparing the prescribed virtual displacement fields (Fig. 6(left)) with the calculated fields shows that the FE-DIC method accurately captures the prescribed heterogeneous displacement field. However, some differences can be seen as a result of the linear interpolation functions of the triangular elements. Furthermore, comparing the difference between the virtual and calculated displacement fields in x and y direction with the displacement field in the z direction shows that the z displacement field is more accurately captured. Thus, the conclusion drawn from the average error in Fig. 5 is confirmed, i.e. the error in the calculated z displacement field is smaller than in x and y direction.

From this error analysis, an optimum element size can be identified. The element size must be sufficiently small to capture the fine-scale fluctuations of the displacement field. However, reducing the element size leads to an increase in the number of degrees-of-freedom, which in turn increases the sensitivity to measurement noise. Based on the error analysis discussed above, the optimum element size
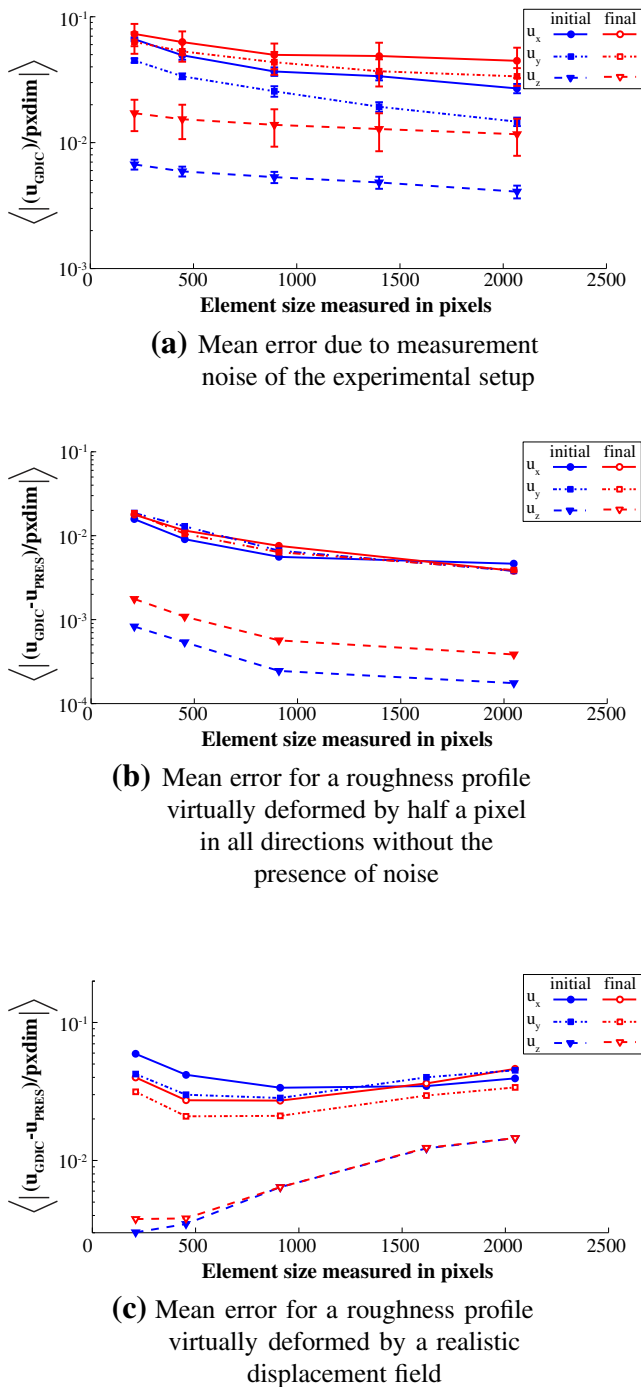
(a) Mean error due to measurement
noise of the experimental setup

(b) Mean error for a roughness profile
virtually deformed by half a pixel
in all directions without the
presence of noise

(c) Mean error for a roughness profile
virtually deformed by a realistic
displacement field

Fig. 5 Mean error in the FE-DIC calculation for three test cases, expressed as a fraction of a pixel, where a pixel is 332 nm

is around 450 pixels per element for the particular problem considered here. This translates to an element size of approximately 10 μm by 10 μm in the case of the confocal optical height profiles used here. For this element size, the average error in the calculated displacement fields is below 10 % of a pixel dimension for both the initial and the final surface profile. The optimal element size is thus relatively large compared to the spatial resolution of the

measured profiles, i.e. the pixel size of 332 nm. Clearly, to reduce the error to a minimum, a large number of data points (pixels) per DOF is required. A smaller element discretization is achievable at the expense of increasing the error.

Proof-of-Principle Experiments

Methodology

The material investigated is a polymer-coated steel known as TH340. The material consists of a continuously annealed, single reduced, DWI (draw-redraw-wall ironing) quality Aluminum-killed low carbon ferritic, electrolytic chromium coated steel (ECCS) sheet, 210 μm thick, lacquered with a protective coating on each side. Tensile samples, with the rolling direction (RD) aligned with the tensile axis, were produced using standard milling. To reduce edge effects, a stack of 5 samples was produced and the top and bottom samples were not used. The tensile samples had a gauge length of 20 mm and a width of 4 mm.

Uniaxial tensile tests show that the material forms a Lüders band after the onset of plasticity, i.e. plasticity initiates in a localization band on one side of the tensile sample, which extends towards the other side. The entire sample deforms plastically after an engineering strain of $\varepsilon \approx 5$ %. Failure of the material occurs at $\varepsilon \approx 19$ %.

The tensile tests were performed on a Kammrath & Weiß micro tensile stage, using a 500 N load cell. The strain rate was set to $5 \cdot 10^{-4} [\text{s}^{-1}]$. The surface profile was measured *in-situ* using a Sensofar PLμ 2300 confocal optical profiler with a 50× objective. The image pixel dimensions are 332 nm × 332 nm. The accuracy of the height measurement is in the order of 20 nm. The experimental setup is shown in Fig. 7.

It is assumed that the thin polymer layer is sufficiently compliant and hence does not influence the roughening of the steel surface. Therefore, the polymer coating is removed prior to the experiment to improve the accuracy of the height measurement of the steel surface. This is accomplished by using N-Methyl-2-Pyrrolidone (NMP) in a two-step process, due to the large amounts of polymer that have to be removed. The NMP is first heated to 80 °C, removing most of the coating. The coating residuals are removed at 130 °C.

The Quasi-3D FE-DIC method requires 1) the presence of an initial surface profile, which is the case here, as shown in Fig. 4(a); and 2) that the contrast change between the two correlated height profiles is small. To guarantee that the second demand is met, an incremental method was adopted. The uniaxial tensile experiments were performed in a stepwise manner. Prior to the tensile test, a height measurement was made on the sample. This defined the FoV for the

Fig. 6 (*left*) Realistic virtual displacement field used in the error calculation; (*right*) displacement fields calculated by the FE-DIC procedure; displacements in microns; *x* direction is horizontal; dashed red line indicates the data region used in the FE-DIC calculation

(a) Virtual u_x

(b) Calculated u_x

(c) Virtual u_y

(d) Calculated u_y

(e) Virtual u_z

(f) Calculated u_z
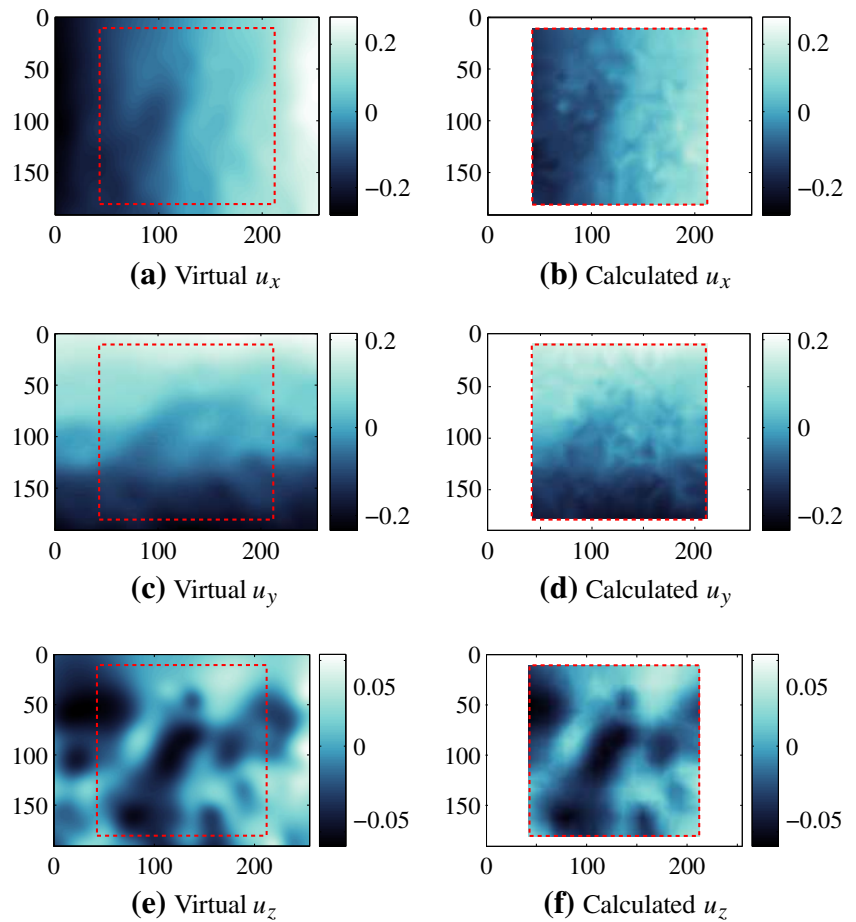
measurement and the undeformed initial roughness. Next, a loading step of $\Delta\varepsilon = 0.25\ \%$ at the prescribed strain rate was performed. Hereafter, a new height measurement was made. The FoV has shifted, as it does not remain centered on the sample. This shift was corrected by comparing the two height profiles and moving the FoV back into view. After this correction step another height measurement was performed, which was stored for later post-processing in the FE-DIC correlation. This completed the measurement cycle and a new incremental loading step was performed. This
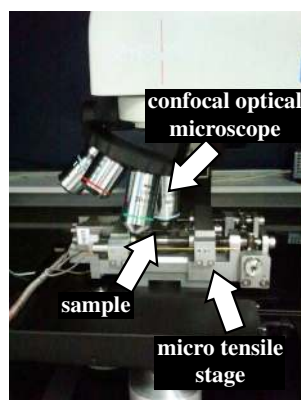

Fig. 7 Experimental setup

process was continued until the material started to fail. Thus, a height profile was measured after each strain increment of $\Delta\varepsilon = 0.25\ \%$, during which the changes in height were progressive and small. This procedure is schematically shown in Fig. 8.

Results

Surface roughness evolution

Height profiles obtained *in-situ* during the tensile test are shown in Fig. 9(left). The initial rolling-induced roughness is shown in Fig. 9(a). Between 0 % and 2.75 % global strain, no real change in surface roughness is noticed, as the material within the FoV deforms elastically, see Fig. 9(c).

Plasticity initiates locally at ∼2.75 % of global (engineering) strain on the sample. This strain is relatively large, due to Lüdering, which delays the local plasticity initiation within the FoV. An abrupt change in roughness appears, i.e. a new roughness pattern overtakes the existing initial surface roughness (Fig. 9(e)). This pattern consists of hills and valleys throughout the FoV. Also visible is a slight rotation of the material within the FoV, due to the formation of a shear band, indicated by the dashed lines.

Fig. 8 Schematic of the incremental FE-DIC calculation procedure; note that the strain increment between two sequential images was $\Delta\varepsilon = 0.25\%$
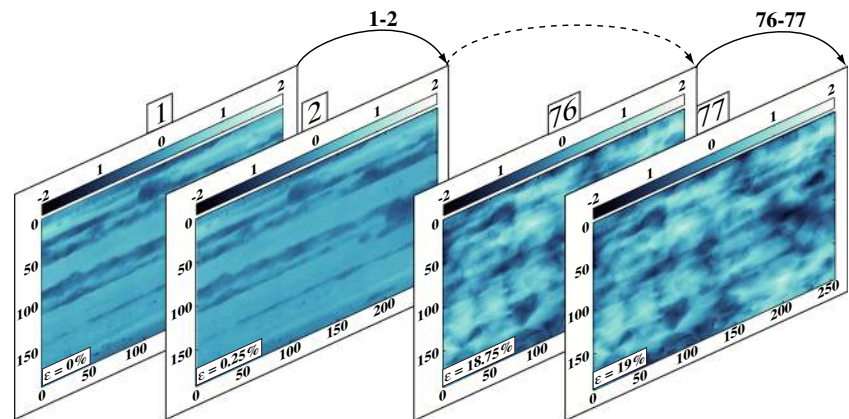
When the strain is increased further, this new roughness pattern grows in height direction, see Figs. 9(g) and (i). The initial surface roughness slowly disappears with increasing deformation, as the new pattern becomes more dominant. No clear formation of new hills and valleys is observed at higher strains. The material slowly realigns the RD with the tensile direction with increasing strain.

Material surface deformation

An initial finite element mesh (see Fig. 9(b)), using linear triangular finite elements, is used to discretize the image of the undeformed height profile (Fig. 9(a)). The element size equals approximately 450 pixels per element, as discussed in section "Verification Analysis". The initial mesh does not cover the full FoV, as a linearly growing displacement is expected in the x direction during the tensile test. FE-DIC calculations are performed in an incremental manner, starting with the initial height profile and the first deformed profile. The latter profile is used as the reference image, $f(\mathbf{x}_0)$, in the next increment. The location of the element nodes is updated between each step. The incremental procedure is schematically shown in Fig. 8. This incremental way of calculating the displacement field leads to an incremental error, as the error from the previous increment is added to the error of a new increment. Another possibility is calculating the displacement field using the initial roughness profile as the reference image. However, the displacement field cannot be determined accurately when the two profiles used in the FE-DIC calculation drastically change, which is the case here (see also Fig. 9). Thus, while using the reference image will initially give accurate results, the accuracy will decrease when the deformation increases.

The FE-DIC discretization at different levels of strains is shown on the right side of Fig. 9. The initial mesh remains more or less undistorted in the elastic regime (Fig. 9(b) and 9(d)). A large mesh update results at the onset of plasticity (Fig. 9(f)). The small rotation noticeable in the experimental height profiles (see the dashed lines in Fig. 9(a) and (e))

is captured by the correlation, see Fig. 9(d) and (f). Further increase in the tensile strain does not lead to significant changes in the mesh. Comparing the discretization close to material failure (Fig. 9(j)) with the initial one (Fig. 9(b)) clearly reveals a positive strain in the x direction (tensile direction) and a negative strain in the perpendicular y direction.
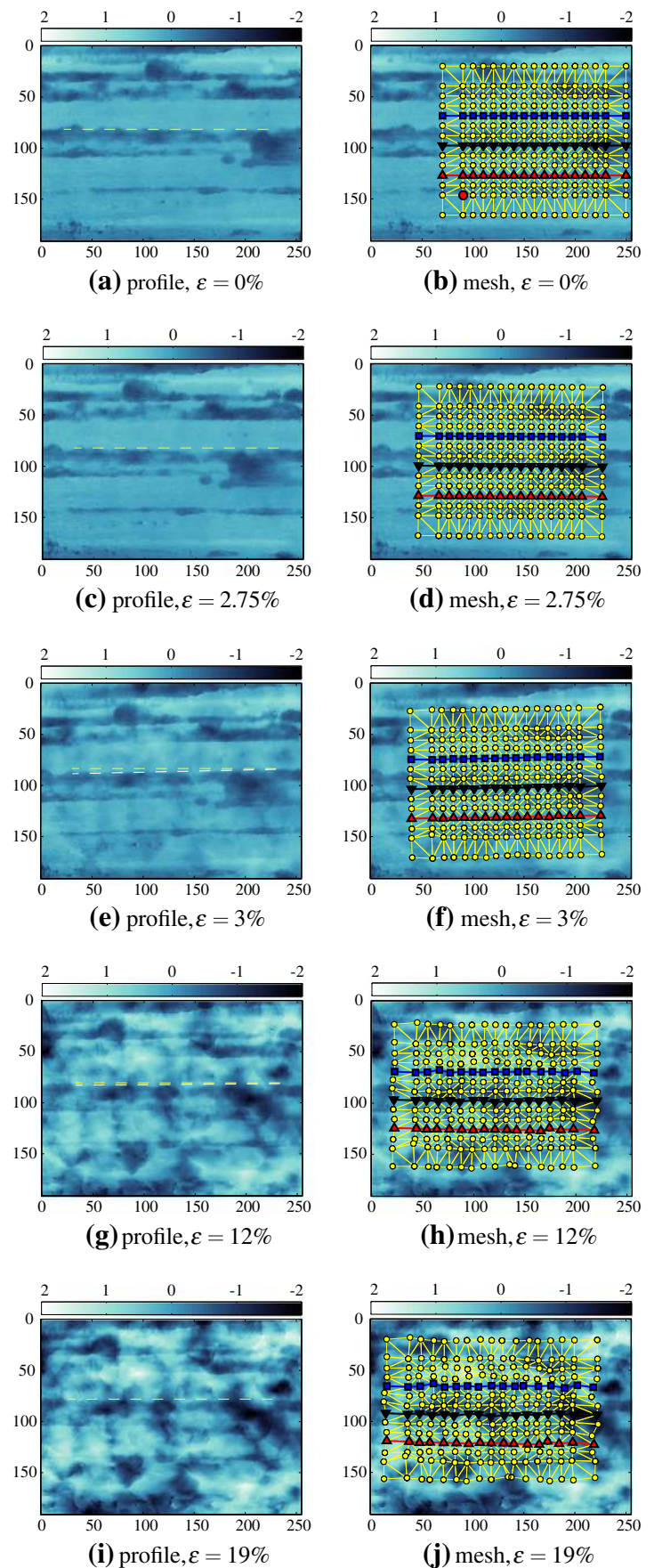
The material displacements in the out-of-plane (z) and tensile direction (x) of the blue, black and red nodes on the right side of Fig. 9 are shown in Fig. 10. The profiles reveal the positive strain in the rolling (tensile) direction, i.e. points on the left side move to the left and vice versa. The hills and valleys formed on the material surface are captured, as well as their growth in amplitude as the strain increases.

The calculated three-dimensional displacement fields for the profiles taken just before and after the onset of plasticity are shown in Fig. 11. The deformation is clearly not homogeneous, as the strain locally fluctuates. The strain in x and y direction can be seen as a displacement gradient in x and y. The rotation seen in the experimental profiles (see the dashed lines in Fig. 9(c) and (e)) is also visible in the gradient, i.e. the gradient is not strictly in RD and TD for x and y, respectively, but rather rotated. The displacement field in z direction clearly shows the formation of hills and valleys during the onset of plasticity.

Note that the displacement field around the red circular node in Fig. 9(b) strongly differs from the surrounding displacement field, see the yellow arrow in Fig. 11(b). This node is initially positioned at an almost vertical slope in the roughness profile. During the onset of plasticity, a new roughness pattern forms over the existing pattern. As a result, the displacement of this node is calculated erroneously, as the node clearly moves away from the material it is supposed to track (see also Fig. 9(f)). Clearly, the FE-DIC calculation is sensitive to a strong vertical slope in the surface profile, because the confocal profiler cannot accurately measure these slopes.

A comparison between the measured roughness profile and the calculated roughness profile for two data lines

Fig. 9 (*left*) Surface height profiles at different strain levels during the tensile experiment, *dashed lines* indicate the local material rotation; (*right*) the corresponding correlated FE-DIC solution; the *blue*, *black* and *red nodal lines* are used in Fig. 10; the *red circular node* shows sensitivity to the steep height change of the initial roughness (see also Fig. 11); all values are in microns, the tensile (*x*) direction is *horizontal* and the *colors* indicate the local height
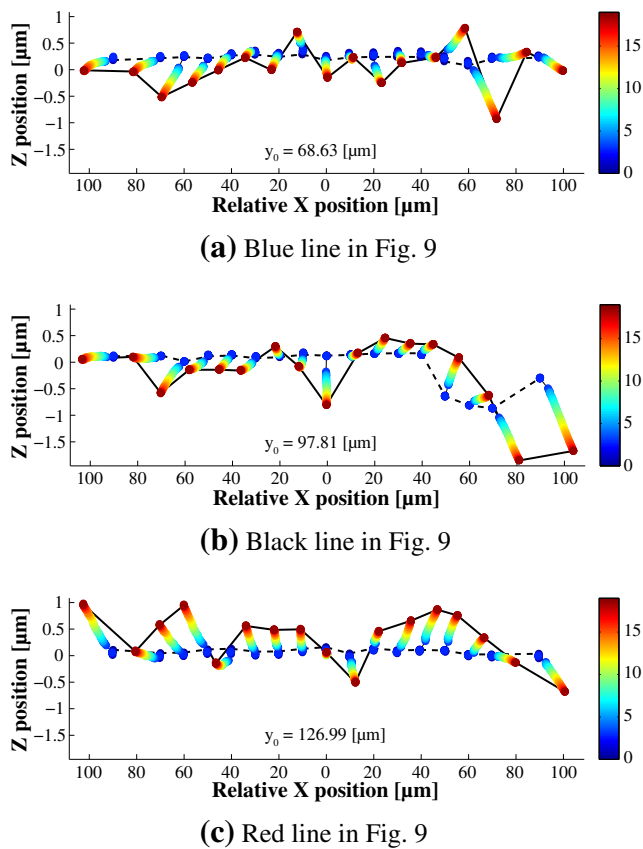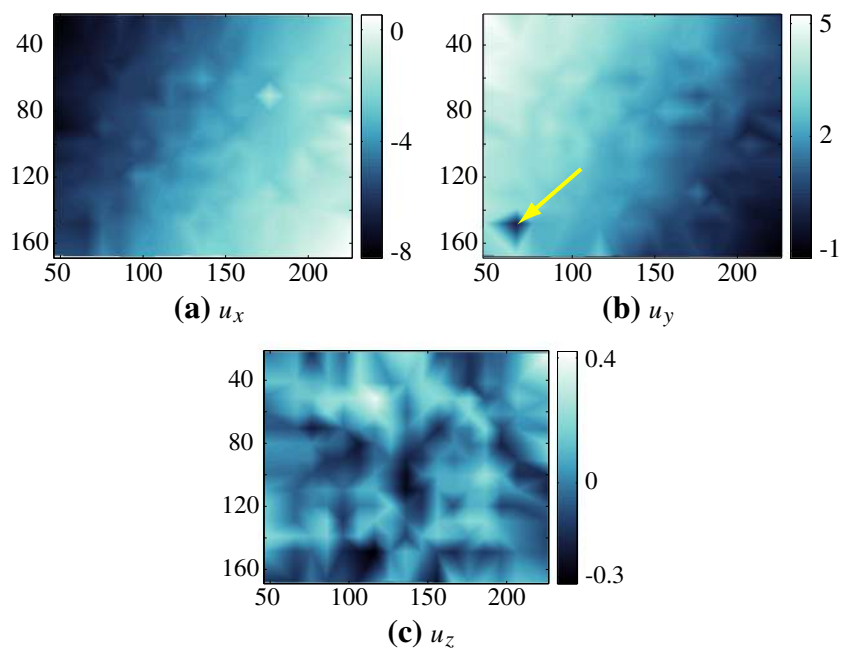

(a) profile, $\varepsilon = 0\%$

(b) mesh, $\varepsilon = 0\%$

(c) profile, $\varepsilon = 2.75\%$

(d) mesh, $\varepsilon = 2.75\%$

(e) profile, $\varepsilon = 3\%$

(f) mesh, $\varepsilon = 3\%$

(g) profile, $\varepsilon = 12\%$

(h) mesh, $\varepsilon = 12\%$

(i) profile, $\varepsilon = 19\%$

(j) mesh, $\varepsilon = 19\%$

(a) Blue line in Fig. 9

(b) Black line in Fig. 9

(c) Red line in Fig. 9

Fig. 10 The evolution of the surface roughness for the *blue*, *black* and *red* nodes (see right side of Fig. 9) in *x* and *z* direction; *colors* indicate the global strain level

perpendicular to the RD at different strains is shown in Fig. 12. The calculated profile was obtained by adding the incremental full-field FE-DIC displacement field to the initial surface profile. In the elastic regime (Fig. 12(a)), the roughness pattern is captured accurately by the FE-DIC calculation. After the onset of plasticity, some differences are seen between the calculated and measured profile. These differences are initially small (Fig. 12(b)), but increase for larger deformation. At the end of the experiment, the calculated and measured profiles show clear differences (Fig. 12(c)). Clearly, some of the small hills and valleys that form are not captured by the finite element discretization. However, the trend in the roughness profile is captured accurately.

Discussion

The error analysis shows that there exists an optimum value for the element size. This obviously limits the resolution of the roughening phenomena that can be resolved in the correlated displacement field. All phenomena that occur at a scale below the element size are constrained by the linear element shape functions. The validity thereof can be assessed in the residual height difference between the measured surface profile and the surface profile obtained with the calculated displacement fields. Examples of this difference were given in Fig. 12. If the element shape functions entirely resolved the real displacement field, only small differences would be visible between the two profiles, i.e. the measurement noise. This is not the case, however, since small peaks and valleys are seen in the measured surface profile, which are not captured by the calculation. Thus,
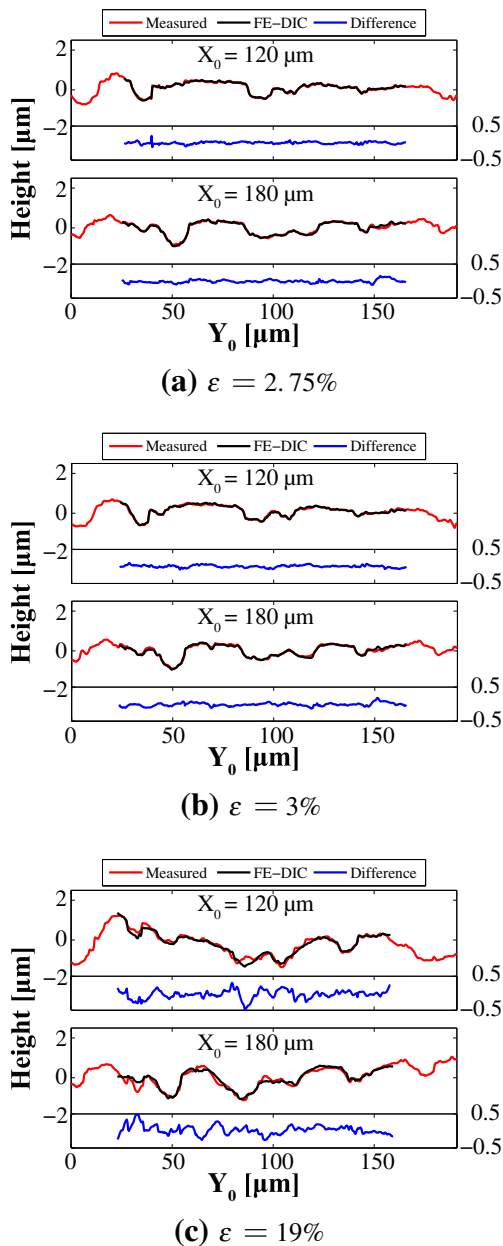
Fig. 11 Calculated displacement fields for the height profiles just before (Fig. 9(d)) and after (Fig. 9(f)) plasticity initiates (around 3 % strain); the *yellow arrow* indicates the location of the red circular node in Fig. 9(b); the values are in microns, the tensile (*x*) direction is *horizontal* and the *colors* indicate the respective displacement amplitudes

(a) u_x

(b) u_y

(c) u_z

Fig. 12 Comparison between a cut out of two lines perpendicular to the RD of the measured roughness profile and the roughness profile which is obtained via FE-DIC displacement fields at different strains during the tensile experiment

the optical resolution is limited by the wavelength of the used light. Non-optical techniques, e.g. AFM, might be used to increase the details in the displacement field that are captured in the correlation. Resolving these fine-scale displacements may be important for some applications, e.g. when a steel surface roughens on a wide range of length scales [4]. Furthermore, an AFM can more accurately measure the steep slopes that are present on the initial surface profile (see also Fig. 9(a)) and thus possibly prevent the error seen in the calculation of the displacement field during the onset of plasticity (see the yellow arrow in Fig. 11(b)).

Another possibility is changing the finite element interpolation. Six-nodal triangular elements look promising, as the shape functions allow for quadratic changes in the displacement field within the elements. Quadratic finite elements have been used in the realistic test case described in section "Verification Analysis" for the final roughness profile (see Fig. 4(b)). The error in the calculation for both linear and quadratic triangular elements is shown in Fig. 13. Comparing the error in *x* and *y* direction shows that the difference between the linear and quadratic elements is relatively small for large elements, while the linear elements out-perform the quadratic elements for small elements. For the *z* displacement error it can be seen that the quadratic elements are more accurate up to small element sizes. The number of degrees-of-freedom per element for the quadratic triangular elements is larger, which leads to an increase in sensitivity to noise. However, for larger elements, the shape functions do allow for a more accurate description of the non-linear out-of-plane displacement field. Thus, depending on the required scale and expected displacement fields, quadratic elements can perform better. Note that the computational cost is significantly increased.

A comparison between the average values of the measured and calculated surface profiles, both for the Root-Mean-Square (RMS, equation (14)) and average (AVG, equation (15)) value, is shown in Fig. 14. Comparing the curves shows that the trend corresponds well. However,
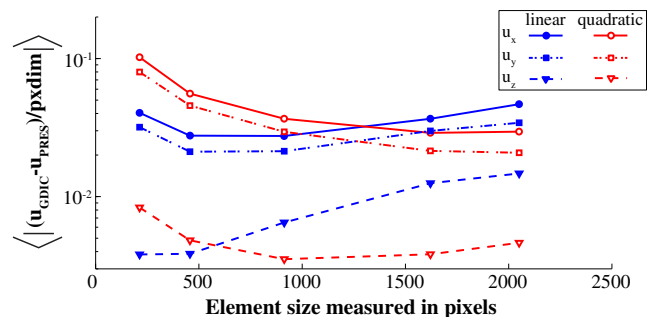
some of the fine-scale details are not fully resolved and hence have to be viewed as non-random noise in the FE-DIC calculation. The elements initially have a size of approximately 10 μm by 10 μm (30 pixels in *x* and *y* direction), which is large compared to these small peaks and valleys.

To resolve these fine-scale details, either the element size or the pixel dimensions have to be reduced. The former gives rise to a larger correlation error, as discussed in section "Verification Analysis", whereas the latter depends on the imaging by the confocal optical microscope, i.e.

Fig. 13 Comparison of the mean error for linear and quadratic elements for a roughness profile virtually deformed by a realistic displacement (see also section "Verification Analysis")
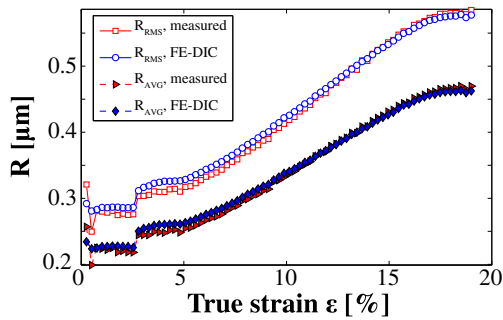
Fig. 14 Comparison between the average values (RMS and AVG) of the height profiles obtained via the calculated displacement fields and the experimental profiles

clear differences between the average values can be seen, especially at relatively small strains. These differences are explained by the finite element discretization. The element size is larger than some of the fine-scale details of the roughening phenomena. These fine-scale details initially contribute to the average surface values, thus explaining the difference. At large strains, the large-scale roughening phenomena dominate the average values. These phenomena are accurately captured by the FE-DIC calculation and thus the average values overlap. A comparison for the height-height correlation and the maximum peak-to-valley (MPV) value is not shown here, as the conclusion drawn is the same.

$$R_{RMS} = \sqrt{\langle \underset{\sim}{f}^2 \rangle} \qquad (14)$$

$$R_{AVG} = \langle |\underset{\sim}{f}| \rangle \qquad (15)$$

Correlating the height profiles before and after the onset of plasticity (see Fig. 9(c) and (e)) was difficult. In the elastic regime, the roughness pattern remains relatively constant (simple stretching only). This initial roughness pattern drastically changes in the plastic regime, where hills and valleys form at the surface. Correlating this sudden change in overall pattern is difficult, especially for fine meshes, due to the large number of degrees-of-freedom involved. The current experiment was performed stepwise with strain increments of $\Delta \varepsilon = 0.25$ %. This step size can be reduced in order to increase the number of height profile images during the early stages of plasticity and thereby decrease the amplitude of the incremental height changes.

Finally, we note that the adopted incremental FE-DIC calculation technique (see Fig. 8) is prone to an incremental error. Different techniques have been developed in an attempt to decrease this error, e.g. the work of Tang et al. [28]. These methods may reduce this incremental error, while still being capable of calculating the displacement field after large changes in contrast have occurred due to the roughening phenomenon.

Conclusion

An experimental surface deformation measurement methodology has been presented, using a Finite Element based Global Digital Image Correlation (FE-DIC) technique. This methodology allows for full-field tracking of material displacements of an evolving surface, both in-plane and out-of-plane. This new way of characterizing an evolving surface height profile provides quantitative information for various surface deformation phenomena, and hence out-performs conventional methods using average height values. However, two requirements have to be met before the technique can be applied, i.e. a) the presence of an initial surface profile, i.e. contrast; and b) a minimal contrast change between the two correlated height profiles.

Accurate information on local material displacements is important in, for example, the case study used in this research. A polymer-coated steel has been investigated, where deformation-induced interface roughening has an important effect on the interface integrity. A proof-of-principle experiment has been performed. The local surface height profile of a sheet metal was measured *in-situ* as it evolves under applied uniaxial deformation and the FE-DIC method was applied to extract the local material displacements of the metal surface. This local deformation field can be used in numerical simulations of roughening-induced interfacial loading problems, directly affecting the local interface integrity.

References

1. Man J, Obrtlík K, Polák J (2003) Study of surface relief evolution in fatigued 316L austenitic stainless steel by AFM. Mater Sci Eng A 351(1–2):123–132
2. Polák J, Man J, Vystavěl T, Petrenec M (2009) The shape of extrusions and intrusions and initiation of stage I fatigue cracks. Mater Sci Eng A 517(1–2):204–211
3. Clarisse L, Bataille A, Pennec Y, Crampon J, Duclos R (1999) Investigation of grain boundary sliding during superplastic deformation of a fine-grained alumina by atomic force microscopy. Ceram Int 25(4):389–394
4. Raabe D, Sachtleber M, Weiland H, Scheele G, Zhao Z (2003) Grain-scale micromechanics of polycrystal surfaces during plastic straining. Acta Mater 51:1539–1560
5. Sachtleber M, Raabe D, Weiland H (2004) Surface roughening and color changes of coated aluminum sheets during plastic straining. J Mater Process Technol 148(1):68–76

6. Thomas TR (1972) Computer simulation of wear. Wear 22(1):83–90

7. van der Aa HCE, van der Aa MAH, Schreurs PJG, Baaijens FPT, van Veenen WJ (2000) An experimental and numerical study of the wall ironing process of polymer coated sheet metal. Mech Mater 32:423–443

8. Boelen B, den Hartog H, van der Weijde H (2004) Product performance of polymer coated packaging steel, study of the mechanism of defect growth in cans. Prog Org Coat 50:40–46

9. van den Bosch MJ, Schreurs PJG, Geers MGD, van Maris MPFHL (2008) Interfacial characterization of pre-strained polymer coated steel by a numerical-experimental approach. Mech Mater 40:302–317

10. Fedorov AV, van Tijum R, Vellinga WP, De Hosson JTM (2007) Degradation and recovery of adhesion properties of deformed metal-polymer interfaces studied by laser induced delamination. Prog Org Coat 58:180–186

11. van den Bosch MJ, Schreurs PJG, Geers MGD (2008) Identification and characterization of delamination in polymer coated metal sheet. J Mech Phys Solids 56:3259–3276

12. Schwerdtfeger J, Nadgorny E, Koutsos V, Blackford JR, Zaiser M (2010) Statistical heterogeneity of plastic deformation: an investigation based on surface profilometry. Acta Mater 58(14):4859–4870

13. van Tijum R, Vellinga WP, De Hosson JTM (2007) Adhesion along metal-polymer interfaces during plastic deformation. J Mater Sci 42:3529–3536

14. Hild F, Roux SG (2006) Digital image correlation: from displacement measurement to identification of elastic properties - a review. Strain 42(2):69–80

15. Bartali AE, Aubin V, Degallaix S (2009) Surface observation and measurement techniques to study the fatigue damage micromechanisms in a duplex stainless steel. Int J Fatigue 31:2049–2055

16. Pan B, Qian K, Xie H, Asundi A (2009) Two-dimensional digital image correlation for in-plane displacement and strain measurement: a review. Meas Sci Technol 20:062001

17. Sutton MA, Orteu J-J, Schreier H (2009) Image correlation for shape, motion and deformation measurements: basic concepts, theory and applications. Springer, New York

18. Tasan CC, Hoefnagels JPM, Geers MGD (2010) Microstructural banding effects clarified through micrographic digital image correlation. Scripta Mater 62(11):835–838

19. Uchida M, Tada N (2011) Sequential evaluation of continuous deformation field of semi-crystalline polymers during tensile deformation accompanied by neck propagation. Int J Plasticity 27:2085–2102

20. Hild F, Roux SG (2012) Comparison of local and global approaches to digital image correlation. Exp Mech 52(9):1503–1519

21. Bay BK, Smith TS, Fyhrie DP, Saad M (1999) Digital volume correlation: three-dimensional strain mapping using X-ray tomography. Exp Mech 39:217–226

22. Vendroux G, Knauss WG (1998) Submicron deformation field measurements: part 2. Improved digital image correlation. Exp Mech 38:86–92

23. Knauss WG, Chasiotis L, Huang Y (2003) Mechanical measurements at the micron and nanometer scales. Mech Mater 35:217–231

24. Han K, Ciccotti M, Roux SG (2010) Measuring nanoscale stress intensity factors with an atomic force microscope. Europhys Lett 89(6):66003

25. Besnard G, Hild F, Roux SG (2006) Finite-element displacement fields analysis from digital images: application to Portevin-Le Châtelier bands. Exp Mech 46(6):789–803

26. Gao Z, Wang Y, Gioia G, Cuitiño AM (2002) A global approach for digital speckle correlation. In: Proceedings SEM Annual Conference

27. Leclerc H, Périé JN, Roux SG, Hild F (2009) Integrated digital image correlation for the identification of mechanical properties. In: Gagalowicz A, Philips W (eds) MIRAGE 2009. LNCS, vol 5496. Springer, Berlin, pp 161–171

28. Tang Z, Liang J, Xiao Z, Guo C (2012) Large deformation measurement scheme for 3D digital image correlation method. Opt Laser Eng 50:122–130